

UC Santa Cruz

UC Santa Cruz Previously Published Works

Title

Implementation and application of the peak scaling method for temperature measurement in the laser heated diamond anvil cell

Permalink

<https://escholarship.org/uc/item/60f4q4s8>

Journal

Review of Scientific Instruments, 89(8)

ISSN

0034-6748

Authors

Kunz, Martin
Yan, Jinyuan
Cornell, Earl
[et al.](#)

Publication Date

2018-08-01

DOI





10.1063/1.5028276

Peer reviewed

Implementation and application of the peak scaling method for temperature measurement in the laser heated diamond anvil cell

Cite as: Rev. Sci. Instrum. **89**, 083903 (2018); <https://doi.org/10.1063/1.5028276>

Submitted: 08 March 2018 . Accepted: 15 July 2018 . Published Online: 10 August 2018

Martin Kunz , Jinyuan Yan, Earl Cornell , Edward E. Domning, C. Ethan Yen, Andrew Doran , Christine M. Beavers , Aaron Treger, Quentin Williams, and Alastair A. MacDowell



View Online



Export Citation



CrossMark

ARTICLES YOU MAY BE INTERESTED IN

[A CO₂ laser heating system for in situ high pressure-temperature experiments at HPCAT](#)

Review of Scientific Instruments **89**, 083901 (2018); <https://doi.org/10.1063/1.5040508>

[Contributed Review: Culet diameter and the achievable pressure of a diamond anvil cell: Implications for the upper pressure limit of a diamond anvil cell](#)

Review of Scientific Instruments **89**, 111501 (2018); <https://doi.org/10.1063/1.5049720>

[A laser heating facility for energy-dispersive X-ray absorption spectroscopy](#)

Review of Scientific Instruments **89**, 013111 (2018); <https://doi.org/10.1063/1.5010345>



MCL
MAD CITY LABS INC.

AFM & NSOM Nanopositioning Systems Micropositioning Single Molecule Microscopes

Implementation and application of the peak scaling method for temperature measurement in the laser heated diamond anvil cell

Martin Kunz,¹ Jinyuan Yan,^{1,2} Earl Cornell,¹ Edward E. Domning,¹ C. Ethan Yen,^{1,3,4} Andrew Doran,¹ Christine M. Beavers,^{1,2} Aaron Treger,¹ Quentin Williams,² and Alastair A. MacDowell¹

¹*Advanced Light Source, Lawrence Berkeley National Laboratory, Berkeley, California 94720, USA*

²*Earth and Planetary Sciences Department, University of California, Santa Cruz, California 95064, USA*

³*Berkeley High School, 1980 Allston Way, Berkeley, California 94704, USA*

⁴*University of California, Berkeley, California 95720, USA*

(Received 8 March 2018; accepted 15 July 2018; published online 10 August 2018)

A new design for a double-sided high-pressure diamond anvil cell laser heating set-up is described. The prototype is deployed at beamline 12.2.2 of the Advanced Light Source at Lawrence Berkeley National Lab. Our compact design features shortened mechanical lever arms, which results in more stable imaging optics, and thus more user friendly and more reliable temperature measurements based on pyrometry. A modification of the peak scaling method was implemented for pyrometry, including an iterative method to determine the absolute peak temperature, thus allowing for quasi-real time temperature mapping of the actual hotspot within a laser-heated diamond anvil cell without any assumptions on shape, size, and symmetry of the hotspot and without any assumptions to the relationship between fitted temperature and peak temperature. This is important since we show that the relationship between peak temperature and temperature obtained by fitting the Planck function against the thermal emission spectrum averaged over the entire hotspot is not constant but depends on variable fitting parameters (in particular, the size and position of the fitting window). The accuracy of the method is confirmed through measuring melting points of metal wires at ambient pressure. Having absolute temperature maps in real time allows for more differentiated analyses of laser heating experiments. We present such an example of the pressure variations within a heated hotspot of AgI at a loaded base pressure of 3.8 GPa. *Published by AIP Publishing.* <https://doi.org/10.1063/1.5028276>

I. INTRODUCTION

The laser-heated diamond anvil cell (LHDAC) has become an important tool in the quest to interpret seismologically derived density and velocity profiles of the Earth with mineralogical models. This is because of its ability not only to simulate conditions of the deep Earth but also to probe them with a variety of methods (including X-rays, visible to IR light, and ultrasonic probes).^{1–6} For this reason, laser-heating facilities have proliferated within both, facilities and individual investigator laboratories; for example, beamline 12.2.2 at the Advanced Light Source (ALS) installed a double sided axial infrared laser heating set-up in 2004.⁷ Precise and accurate measurements of pressure and temperature are crucial for the LHDAC to be useful. Pressure can be determined using independent methods, such as ruby fluorescence,⁸ or equations of state of various suitable materials.^{9,10} Measuring accurate temperatures of a laser-heated sample, however, is an ongoing problem. So far, all methods deployed involve some more or less sophisticated flavor of spectroradiometry, which is based on fitting a Planck or Wien equation to the measured thermal radiation of the hotspot.^{11–13} Factors affecting the reliability of these methods include experimental limitations such as the precise and stable alignment of collection optics on the peak hotspot, chromatic aberration,^{14,15} optical effects of diamonds,¹⁶ as well as sample specific effects such as unknown emissivities (including possible deviations from grey-body

emission),¹⁷ and axial and radial temperature gradients.^{18–20} In the recent past, numerous remedies have been proposed and tested to circumvent one or several of these limitations. These include using reflective instead of refractive optics,²¹ sophisticated quantification of chromatic effects specific to an individual set-up,^{14,16,21} minimizing thermal gradients through shifting the intensity profile of the incident laser beam, or multispectral imaging radiometry.¹³ In the last approach, four narrow bandpass images at four different wavelengths are collected across the entire hotspot. This yields four intensity maps, which are carefully spatially correlated. For each pixel of the covered area, a Planck function is fitted against the four measured intensities at that particular pixel. This gives a 2-dimensional temperature map, as well as a map of the temperature dependent grey-body emissivity. While this method is an ingenious way to solve many of the above-mentioned problems in one strike, it is non-trivial to implement at a user facility with its specific demands of alignment robustness and near-real-time results. The differences between a user facility such as a synchrotron beamline and a dedicated laser heating lab at a university laboratory are two-fold; the utilization of a given sample stage where the laser heating set-up is installed with a variety of user-specific experimental environments not related to laser heating requires frequent rebuilding, which leads to unwanted disturbances of a delicately aligned set-up. In addition, a publicly accessible facility is operated by a variety of users with vastly different skill sets and experimental

talents, which again often leads to unwanted disturbances of carefully aligned equipment. An installation at a user facility is therefore much more than a state of the art university research lab instrument. The facility instrument has to satisfy very high demand in terms of alignment stability and ease and speed of realignment.

The peak-scaling method as proposed by Kavner and Nugent²⁰ and Rainey and Kavner²² preserves the 2-dimensional mapping characteristics of the multispectral imaging radiometry but at the same time simplifies the experimental set-up and re-alignment procedure, allowing the user facility to offer a freshly aligned instrument to each of its ca. 30–50 annual users, and—most importantly—removes any chromatic aberration issues. The peak-scaling method relies on summing the entire hotspot's spectral output into a single image and analyzing it with one spectrometer. This averages the 3-dimensional oblate temperature distribution of the hotspot within a dielectric or the primarily 2-dimensional distribution at a metal's surface into a single spectrum that is sufficiently similar to a Planck curve that it can be used to extract a temperature by fitting the Planck or Wien function to it. Note here that due to the spatially indiscriminate collection and averaging of the full hotspot's emissions, chromatic aberrations are completely avoided. We emphasize that this aspect of the peak scaling method represents perhaps its biggest strength. Fitting a Planck curve to this single observed, hotspot-summed spectrum yields a temperature that is slightly lower than the peak temperature due to the surrounding lower temperature regions that contaminate the signal from the more intensely emitting, highest temperature zone (chromatic mixing). However, by combining this single observed spectral curve with an intensity map of the hotspot recorded at a single well known wavelength allows not only for the determination of the real peak temperature associated with the observed hotspot but indeed for the establishment of an absolute temperature of each pixel across the full 2D image of the hotspot without any prior assumptions, e.g., with respect to the exact relationship between fitted chromatically mixed temperature and peak temperature. The advantages of this method compared to multispectral image radiometry are that it is relatively insensitive to precise alignment of the collection optics, and it is relatively easy and quick to realign in the case of operator abuse. These make this method far more robust for use in an environment, in which a variety of different DAC designs and a wide range of user skill sets are present, as is typical of a synchrotron beamline facility. Moreover, this method delivers rapid, virtually instantaneous information on peak temperature and temperature distribution, thus allowing real-time experimental adjustments or modification.

The original challenge of the peak-scaling method is that it requires *a priori* knowledge of the relationship between the peak temperature of the hotspot and the temperature fitted against the averaged spectrum of the entire hotspot. Rainey and Kavner²² employ sophisticated modeling to show that the ratio between peak temperature and modeled average temperature is relatively insensitive to experimental conditions and the nature of the sample (and particularly whether the sample is insulating or metallic). Kavner and Nugent²⁰ and Rainey and Kavner²² also explore the effects of the “*a priori*” unknown emissivity

on the determined average temperature. In our new approach, we do not need any *a priori* knowledge of the relationship between fitted temperature and peak temperature. Instead, we use the monochromatic intensity image of the hotspot as a second piece of information, which allows us to derive a correctly scaled absolute temperature not only of the peak temperature but also for every pixel of the entire recorded hotspot.

Here, we first describe the laser heating set-up as implemented on ALS beamline 12.2.2 (Sec. II), which allows for quasi-real-time temperature mapping based on the peak scaling method. We then show in Sec. III that the temperature obtained by fitting the Planck function against the averaged spectrum of the entire hotspot and the peak temperature needed to establish the temperature map can vary depending on the fitting parameters chosen, therefore requiring an approach independent of assumptions with respect to the fitted temperature and peak temperature. In Sec. IV, we present such an approach; an iterative quasi-real-time method to determine the correct scale factor and thus an absolute temperature map without prior assumptions and approximation of the relationship between fitted temperature and the peak temperature. This is the method that has been implemented on beamline 12.2.2 at the Advanced Light Source (ALS) of the Lawrence Berkeley Lab (LBL) in Berkeley.

In the final Sec. V, we present how a temperature map combined with diffraction data can be used to measure the spatial distribution of thermal pressure in a diamond anvil cell. The thermal pressure is not only a thermodynamically important parameter, reflecting a combination of the thermal expansion and bulk modulus, but its magnitude also can reveal whether the behavior of a heated sample in the diamond cell can be treated isochorically, isobarically, or as taking an intermediate thermodynamic path.

II. IMPLEMENTATION AT 12.2.2

The peak scaling method was implemented on 12.2.2 in conjunction with a complete rebuild of the *in situ* laser heating set-up. Upstream and downstream laser heating and spectroradiometry optics for this double-sided heating set-up are mounted on opposite surfaces of a 1 × 1 m breadboard, which is mounted perpendicular to the incoming X-ray beam to the right side (looking downstream) of the sample position. A schematic of the downstream set-up is displayed in Fig. 1; the upstream set-up is symmetrical on the opposite side of the breadboard.

A 1090 nm IR fiber laser (SPI SP-100C-0017) (1) is focused onto the sample position (3) through 2 IR mirrors, 2 beamsplitters and an 80 mm f/2.85 apochromatic objective lens (4) by Jenoptik Inc. The last 2-in. diameter beamsplitter (5) is motorized, thus allowing fine adjustments of the laser hotspot independent of the spectroradiometry alignment. The image of the hotspot is collimated through the same objective lens (4) and then focused through an achromatic 1 m lens (7), 3 mirrors (6), and an optical fiber into an OceanOptics Jaz spectrometer (11). The last mirror (10) is motorized, thus allowing a remote optimization of the spectrometer signal without affecting the hotspot position. Along the way, the image passes through two beamsplitters, which direct the

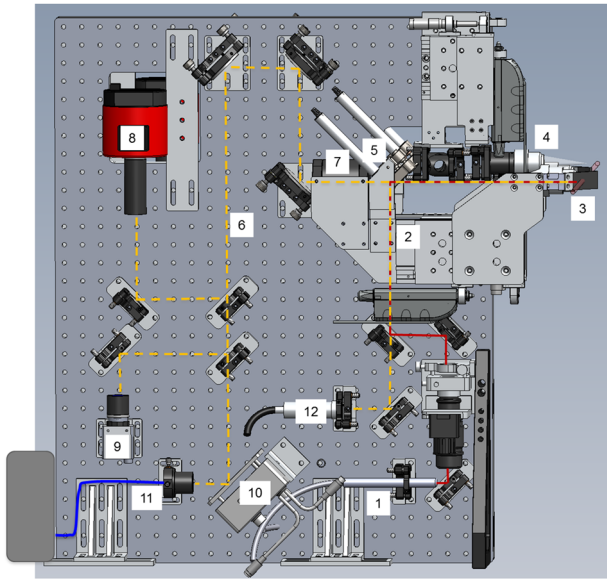


FIG. 1. Schematic of downstream installation for peak scaling pyrometry on ALS beamline 12.2.2. 1090 nm fiber laser collimator head (1), IR path (red) (2), sample position (3), 80 mm $f/2.8$ objective lens (4), motorized IR mirror (5), transparent for visual image and pyrometry beam paths (yellow) (6), achromatic 1 m imaging lens (7), monochromatic 14 bit camera with 700 nm notch filter (8), 8 bit color GigE camera (9), motorized remotely controlled mirror (10), pyrometry signal fed into OceanOptics Jaz spectrometer via optical fiber (11), light source for sample illumination (12).

image onto a monochrome 14 bit BigEye camera equipped with a 700 nm notch filter (8) and an 8 bit color GigE camera (9), respectively. The 14 bit monochromatic camera creates the image that is the basis for the temperature map; the color camera is for sample and hotspot visualization for alignment purposes. The compact design of the optical path minimizes mechanical lever arms and thus greatly reduces remnant vibrations. This leads to a greatly increased stability of the hotspot and consequently reduces uncertainties in the temperature determination.

Experimental control, data acquisition and analysis as well as user interface are integrated into the existing ALS LabView control system. The laser power and position control [Fig. 2(a)] is separated from the temperature measurement interface [Fig. 2(b)].

The laser position control allows for a fine-stepped adjustment of the IR laser position based on the image of the visible glow of the hotspot. After alignment of both the upstream and downstream hotspots into the center of the field of view, and on top of each other using mirror (5), the spectral signal can be maximized by adjusting mirror (9). The co-location of the center of the laser hotspot ($\sim 30 \mu\text{m}$ FWHM) onto the X-ray spot ($\sim 10 \mu\text{m}$ FWHM) is achieved by aligning the X-rays with respect to an absorption fiducial (e.g., the center of the gasket hole) and subsequently aligning the laser and spectrometer onto the same position. Once aligned, the relative position is maintained and the relative position of the hotspot within the sample chamber is varied using the sample stages without touching the mutual alignment of X-rays, laser hotspot, and spectrometer.

The pyrometry is fully automated within the LabView control system. The user has the choice between acquiring

only a single temperature corresponding to a fit of the Planck function against the spectral curve obtained from averaging over all pixels of the imaged hotspot or refining a full temperature map for the observed hotspot. A single mouse click initiates data acquisition, automatic data reduction (correction for optical transfer function, linearization), and temperature fit as well as temperature map calculations. The cycle time for a single temperature fit is quasi-instantaneous and is usually found to be below 5 s.

In our implementation of the spectroradiometric temperature fitting, we employ a standard normalized version of Wien's approximation of the Planck function:

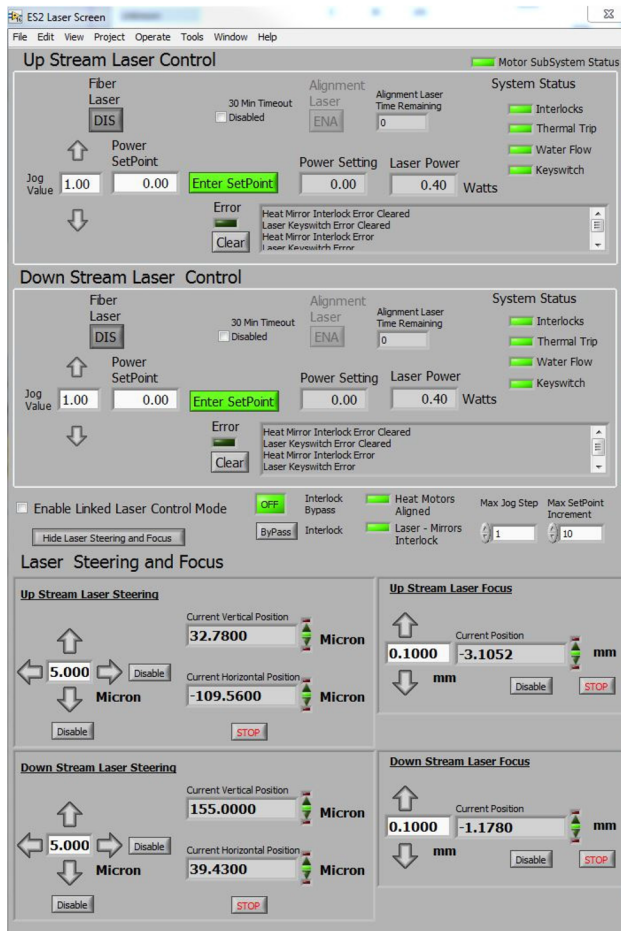
$$I = \ln\left(\frac{I(\lambda)\lambda^5}{2\pi \cdot c^2 h}\right) = \ln \varepsilon - \frac{hc}{k\lambda T}. \quad (1)$$

Here, ε is the emissivity, I is the intensity, and λ is the wavelength. Note that Wien's approximation ($e^{\frac{hc}{k\lambda T}} \gg 1$) is valid for the common experimentally accessible wavelength range (200–1000 nm) and for temperatures up to ~ 6000 K. A linear fit to this curve gives a slope that is the inverse of the temperature and an intercept that corresponds to the natural logarithm of the effective emissivity. In practice, the fitting is chosen to be restricted to the $(hc/k\lambda)$ range, where the normalized curve shows the lowest scatter and smallest deviation from linearity. The operator can interactively optimize the spectrometer and video camera acquisition times to avoid saturation or under-exposure, as well as the wavelength window within which spectral data are used for the temperature fit. Calibration files for optical transfer function are chosen for the relevant temperature range. They are created using a calibrated tungsten ribbon filament lamp (The Pyrometer Instrument Company, Inc., Model STL-H) positioned at the sample position. The calibration is stable and is redone about 2–3 times a year. Raw and corrected data, calibration data, laser power settings, and fitting parameters as well as monochromatic images of hotspot and temperature maps are automatically stored with an incrementing filename, such that a user can easily collect several temperature measurements in rapid sequence during a heating cycle by simple repeated mouse clicks. The accuracy of the temperatures derived were verified by the ambient pressure melting point of 0.25 mm thick wires of Ni, Pt, and W.⁷ The measurements captured the highest temperatures before melting-induced wire failure. These temperatures were found to be between 3% and 6% below the theoretical melting temperatures. This is a good corroboration of the accuracy of our temperature measurements since the wire melt event happened as a run-away process which was difficult to capture at the precise failure moment.

III. MODELING OF FACTORS AFFECTING THE FITTED TEMPERATURE

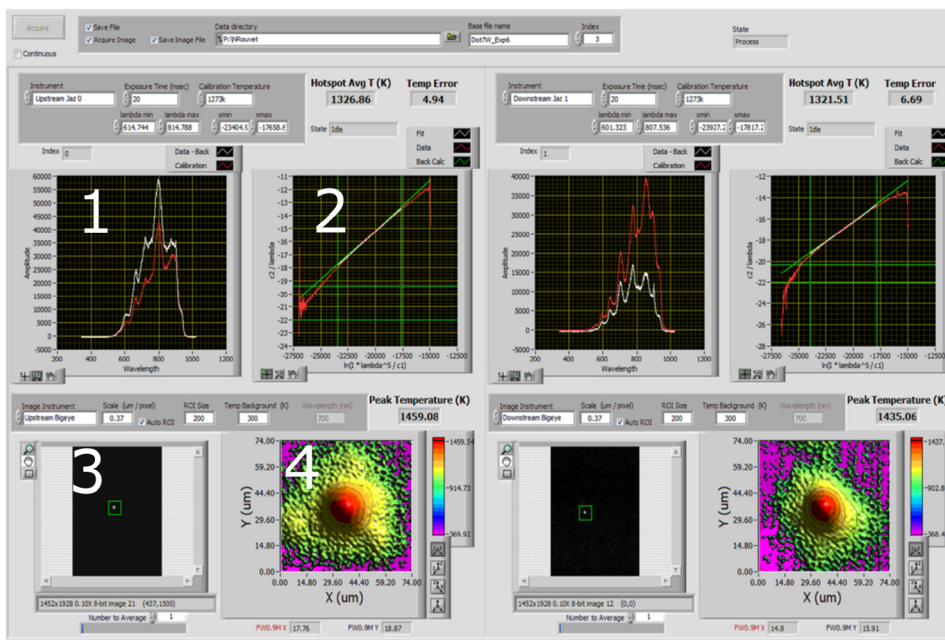
A. Method

The interactive adjustment of the wavelength window has an effect on the temperature obtained from fitting a Planck function against the pseudo Planck curve obtained from the intensity averaged spectrum from the entire hotspot. Conceptually, this is because a spectral fitting window that



(a)

FIG. 2. (a) LabView Interface for laser power and position control. (b) The pyrometry user interface shows on the top panels for up (left)- and downstream (right) raw data (white) on top of the calibration curve (red) in (1), next to the normalized plot (red) and its fit (white) in (2). The top panel gives the temperature fitted to the averaged spectrum (1) of the entire hotspot. The user can select the spectrometer exposure time and interactively adjust the fitting wavelength window to the linear region within the normalized plot. The bottom panels show the 700 nm 14 bit image (3) with the ROI (green square) on which the temperature is mapped (4). The peak temperature given in the bottom panels is iteratively optimized such that the fit-temperature calculated for the temperature map equals the temperature fitted to the observed hotspot.



(b)

extends to smaller wavelengths will have a greater representation from higher temperatures in the composite averaged spectrum of the thermal emission from the entire hotspot; an extension to higher wavelengths will produce the opposite bias.

To explore the dependence of temperatures deduced from spectroradiometric data on the fitting procedure, we worked with a “synthetic” model hotspot as well as a “synthetic” spectrometer initially proposed and applied by Heinz and Jeanloz.¹² All modeling calculations were performed using

custom written scripts within Matlab²³ which can be obtained from the author upon request.

The synthetic hotspot that we utilize has the form of a 2-dimensional function (Gaussian), with variable width and variable pixelation (this shape is in accord with that generated by a sample heated by a laser tuned in TEM00 mode). The default pixelation consists of a grid of 201×201 pixels compared to typical hotspot widths of 30 pixels, i.e., clearly large enough to ensure that locations beyond the edge of the grid have negligible intensities. Each pixel was assigned a finite temperature depending on the assumed peak temperature and width. The chosen default pixelation was chosen to be fine enough by an order of magnitude to avoid any artifacts due to pixel interpolations. The entire grid represents the image that is fed as a whole into the synthetic single line spectrometer. This means that our synthetic spectrometer sees a radiative input consisting of the average of all 201×201 temperatures from the synthetic grid. Calculations were done by varying the spectral window employed for the temperature fitting of an assumed hotspot of 2000 K peak temperature with a width of about 15% of the imaged window, i.e., very close to the experimental situation at ALS beamline 12.2.2, and compatible with those deployed by a number of other spectroradiometric LHDAC temperature measurement systems.

B. Results: Factors affecting fitted temperatures

The selection of the spectral fitting window has an intrinsic effect on the fitted temperature that is rooted in the fact that the averaged intensity collected from the full hotspot is not a true Planck curve and thus shows significant variation of slope with inverse wavelength in the normalized plot. Figure 3 compares intensity [Fig. 3(a)], normalized intensity from Eq. (1) [Fig. 3(b)] as well as the slopes of the normalized intensity [Figs. 3(c) and 3(d)] for a pixel-averaged hotspot [a 2-D Gaussian with $T(\text{Peak}) = 2000$ K and $\sigma = 30$ pixels], together with a true Planck curve for 2000 K, as well as a proper Planck curve for the temperature obtained by fitting a Planck function against the pixel-averaged spectral curve of the entire hotspot. All curves are calculated with the same emissivity (1 in this case). As can be seen from the Planck intensities [Fig. 3(a)], the Planck curve of the peak temperature is different from the pixel-averaged curve, which in turn overlaps the Planck curve of the fitted temperature closely, albeit not perfectly. When plotting the same curves in their normalized form [Fig. 3(b)], the difference is less apparent, and in fact, the three curves appear to have very similar slopes, which correspond to the inverse of the temperature. Close inspection of the slopes [Fig. 3(c)], however, shows that the Planck curves

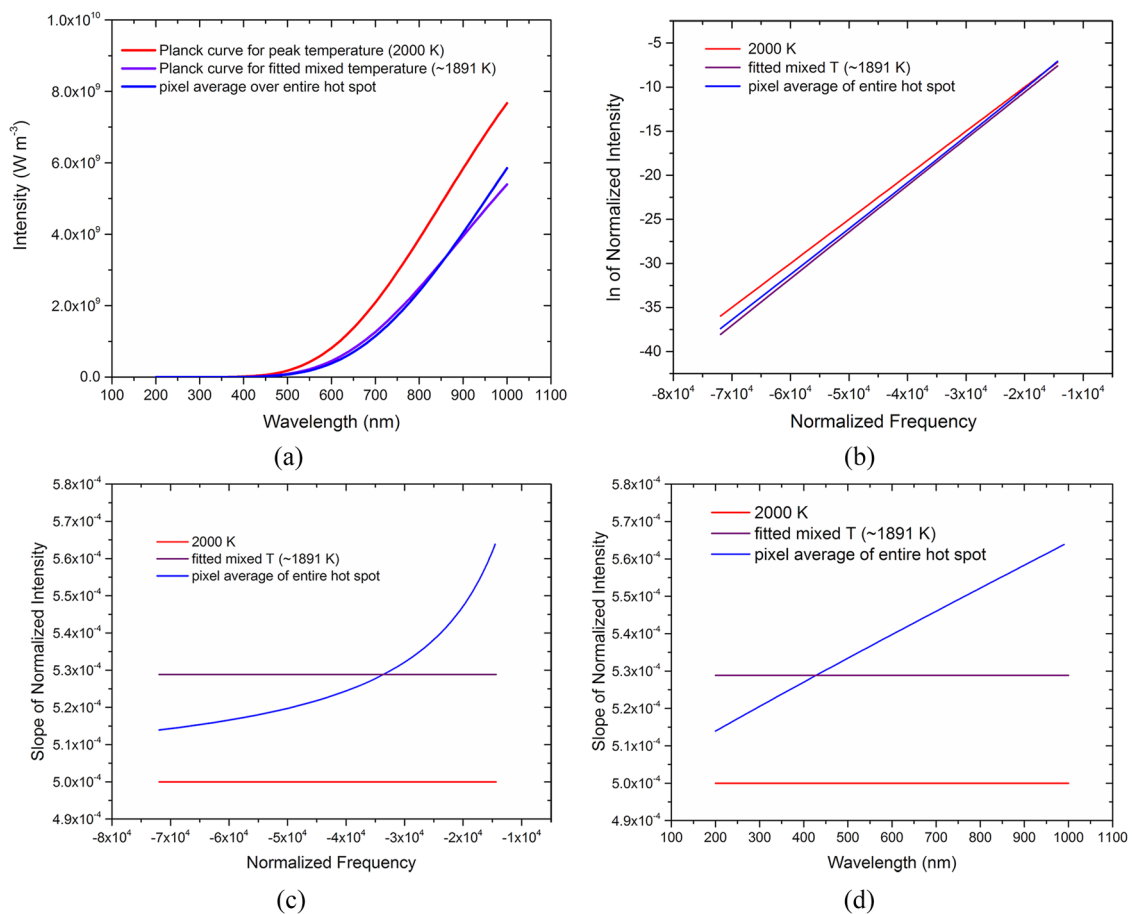


FIG. 3. (a) Spectral curves over the experimentally relevant thermal emission range for a synthetic hotspot. The peak temperature of the hotspot is 2000 K (red). When a Planck curve is fitted against the intensity averaged over all pixels (blue), a temperature of ~ 1891 is obtained (purple). (b) The normalized intensity curves display a linear curve whose slope corresponds to the inverse temperature. [(c) and (d)] The slope of the normalized intensity curves as a function of the normalized frequency (c) and wavelength (d). Note that the normalized curve in (b) obtained by averaging the intensity over all pixels is not linear, and thus its slope depends on what fitting window is chosen.

have a constant slope (as they should have within the Wien approximation), whereas the positive slope of the pixel-averaged spectral curve shows a hyperbolic ($1/x$) decrease against the normalized frequency ($\sim 1/\lambda$) and thus a linear increase with λ [Fig. 3(d)]. From Figs. 3(c) and 3(d), it is apparent that the temperature fitted to the pixel-averaged curve is dependent on what wavelength window is employed.

The peak scaling method produces temperature maps of the hotspot by inverting the intensity map obtained from the high dynamic range monochromatic image of the hotspot. Since the intensity map does not display absolute intensities, it needs to be scaled. One way to properly scale the inverse Planck function is if the intensity-temperature relationship for at least one pixel of the intensity map is known. This is commonly done using the peak temperature of the hotspot. The relationship between the peak temperature and the associated fitted mixed temperature, however, is not constant. Indeed, the difference between peak temperature and fitted temperature from the entire hotspot increases with increasing peak temperature (Fig. 4).

This behavior can be rationalized because while the width of the temperature peak stays constant with varying peak temperatures, the width of the peak in spectroradiometric intensity decreases with decreasing peak temperature, and as a consequence, the averaged intensity across the entire hotspot is more biased towards the peak temperature at lower temperatures (Heinz and Jeanloz,¹² Williams, Knittle, and Jeanloz¹).

The curve in Fig. 4 has been calculated using a broad wavelength range spanning between 200 and 1000 nm in wavelength. This broad of a wavelength range is rarely deployed in practice; measured wavelengths typically span from the visible into the near infrared. During an experiment, the experimental emission curve is pre-processed by dividing the raw spectrum by an instrument response function (see Sec. II). The instrument response function varies greatly across the available spectral range. This, together with other experimental

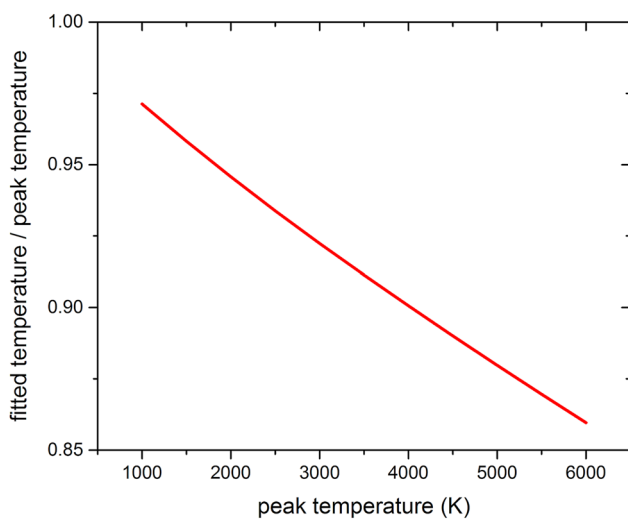


FIG. 4. The relationship between peak temperature and fitted temperature obtained from an average spectrum of the entire hotspot using the full spectral range (200 nm–1000 nm) considered in Fig. 3. This relation is dependent on the peak temperature, with higher peak temperatures yielding a larger discrepancy between fitted temperature and the peak temperature.

phenomena (including that diamonds begin to become significantly more opaque below ~ 250 nm), causes the normalized experimental curve to be affected by higher noise and often deviations from linearity at the edges of the spectrum. For this reason, the wavelength range used for temperature fitting is dynamically adjusted by the user between each run, while ensuring that it is restricted to the linear range.

As documented above, temperature measurements performed with different wavelength fitting windows inherently show different results. The divergence of the curves in Fig. 3(d) causes the temperature fit to the averaged spectrum of the full hotspot to depend on the size and position of the wavelength window used for the fitting. The positive slope of the averaged spectrum in Fig. 3(d) make higher wavelengths bias the measured temperature of the averaged full hotspot towards lower temperatures [the y-axis in Figs. 3(c) and 3(d) is $\sim 1/T$]. This trend can be seen in Fig. 5; the curves represent the temperature fit to the averaged spectrum of a Gaussian hotspot with a width (sigma) of 30 μm and a peak temperature between

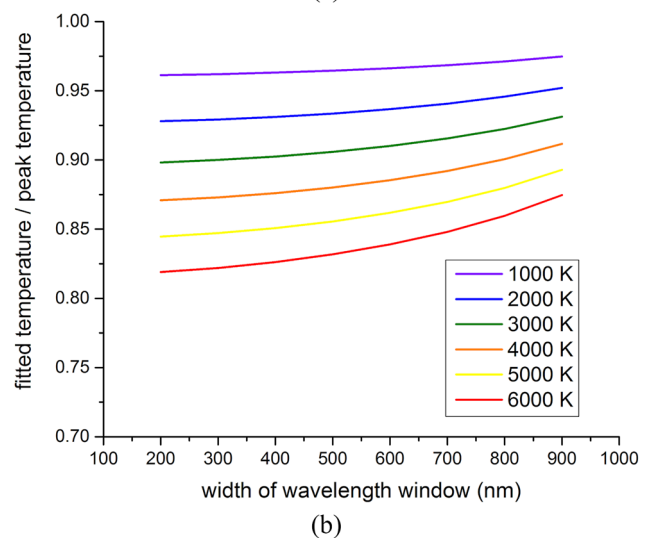
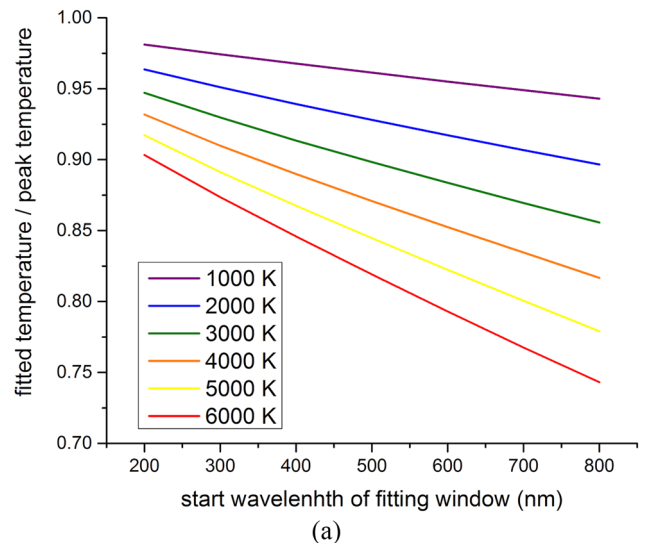


FIG. 5. (a) Dependence on the relationship between fitted temperature and peak temperature on the position of a 200 nm wide wavelength window used in the fit. (b) Dependence of the relationship between fitted temperature and peak temperature on the width of a wavelength window centered around 600 nm.

1000 K and 6000 K as a function of position with a 200 nm wide fitting window. The divergence displayed in Fig. 3(c) is reflected in the ratio of average temperature to peak temperature in Fig. 5(a); this ratio decreases with increasing starting wavelength with slopes increasing from $-0.6 \times 10^{-4} \text{ nm}^{-1}$ (1000 K peak T) to $-2.6 \times 10^{-4} \text{ nm}^{-1}$ (6000 K peak T). The change in size of a fitting window centered around 600 nm leads to a smaller variation in derived average temperature with a slight positive slope, which increases with increasing peak temperature [Fig. 5(b)].

In summary, the ratio between fitted average temperature and peak temperature varies significantly with deviations from as little as a few percent at low temperatures fitted at small wavelength ranges to up to 25% at very high temperatures (6000 K) fitted at large wavelength ranges. In the most commonly accessed temperature range between 2000 and 4000 K, the variation is between 5% and 19%. This variation occurs, simply due to the fitting algorithm, even in the absence of sample dependent issues or experimental artifacts. However, as will be described in detail in Sec. IV, as long as care is taken to utilize identical wavelength windows when analyzing the information derived from the 2D intensity map that is the second ingredient in our method, we arrive at a self-consistent scaling method and are able to derive absolute temperatures insensitive to this experimental parameter. When the entire hotspot is used as an input for spectroradiometric temperature determination, the fitted temperature is surprisingly insensitive to the size of the hotspot. Due to the $I \sim T^4$ relationship which biases the intensities (and thus measured temperatures) heavily towards the central part of the hotspot, we did not find any significant variation in the fitted temperatures up to peaks with FWHM (263 units, i.e., Gaussian $\sigma = 100$ units) exceeding the image size (201 units).

Emissivity greatly affects the radiative properties of any material and its specific effects on measured temperatures within the laser heated diamond anvil cell have been described extensively in the literature^{17,19,20,24–30} including specifically its effect on the peak scaling method.²² Unfortunately, emissivity values (and particularly their dependence on wavelength) are very poorly known for most materials, especially for minerals and rocks (e.g., Touloukian and DeWitt³¹). Estimates suggest a small wavelength dependent variation in our range of interest (200–1000 nm), and a more substantial dependence on temperature between room temperature and temperatures routinely achieved with laser heating.²⁰ Obviously, in our case, the emittance derived from the intercept of the normalized intensity plot from the averaged hotspot provides no direct physical constraint on the material's emittance. In the absence of better data, we perform the temperature fit based on the grey surface/body assumption, i.e., that there is no dependence of emissivity on temperature, wavelength, and emitting angle. We tested in our simulations how a deviation of the material's property from these assumptions affects the derived temperatures. For this exercise, we varied both wavelength- and temperature-dependent emissivity, and a combination of both. We assumed possible emissivity variations between 200 and 1000 nm from 0.25 to 0.4, and from 0.1 to 1 between 300 K and 3000 K. As can be seen from Fig. 6, the temperature dependence of the emissivity—although substantial in magnitude across the

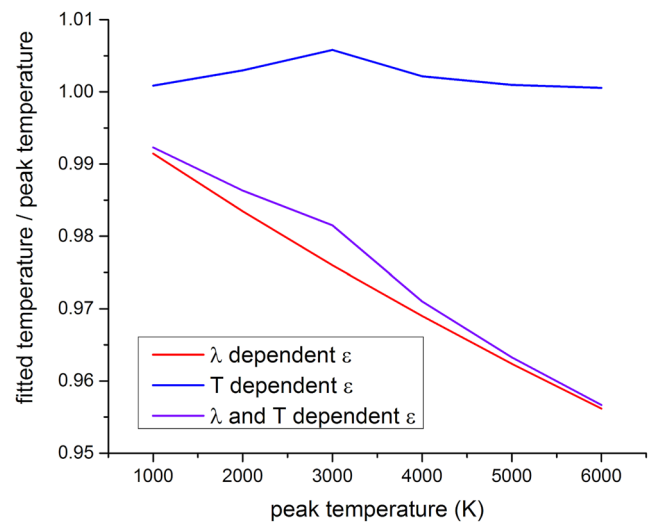


FIG. 6. Relationship between peak temperature and temperature fitted to the averaged spectrum of the entire hotspot for different scenarios of emissivity dependence. Wavelength (λ) dependence is assumed to correspond to an increase in emissivity from 0.25 to 0.4 over the wavelength range (200–1000 nm), and the temperature dependence was set to a positive dependence from 0.1 to 1.0 from 300 to 3000 K and 1 for temperatures larger than 3000 K.

spectrum—has a negligible effect on the fitted hotspot temperature. This is due to the Stefan-Boltzmann relationship, which weighs lower temperature pixels much less than the high temperature ones; in our emissivity model, the high-temperature pixels are less affected. By contrast, the wavelength dependence of the emissivity has a significant effect, reducing the average temperature progressively between 1% and 4% relative to the grey body model for peak temperatures between 1000 and 6000 K. Not surprisingly, a combined model assuming both temperature and wavelength dependence is strongly dominated by the wavelength dependence.

IV. QUASI-REAL-TIME DETERMINATION OF THE PEAK TEMPERATURE

As elaborated in Sec. III B, inverting the monochromatic intensity map to a temperature map requires proper scaling, which could be done unambiguously if the temperature for one pixel of the intensity image, e.g., the peak temperature was known. We also show in Sec. III B that based solely on the temperature fit to the intensity averaged spectrum, a peak temperature is not unambiguously given. However, the experimental procedure of the peak scaling method provides two sets of information, which are sufficient to determine the real scale factor and thus a temperature map representing a true temperature distribution. These two sets of information are (i) the monochromatic intensity map at a single wavelength (for this example, 700 nm) and (ii) the temperature fitted to the averaged spectral curve of the entire hotspot. If the temperature map inverted from the 700 nm intensity map displays correct absolute temperatures, the temperature obtained by fitting a Planck function against the averaged intensities of the temperature map will be equal to the temperature fitted to the averaged spectrum of the observed hotspot as long as in both steps the same wavelength window is used. The difference

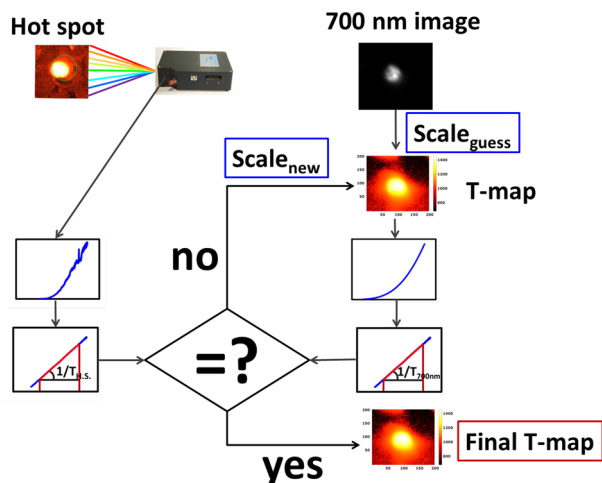


FIG. 7. Sketch illustrating the iterative procedure to obtain the correct scale factor and thus a temperature map with correct absolute temperatures.

between these two values is thus the cost function to be minimized during the iterative process where the scale factor is the variable adjusted. The iterative procedure is illustrated in Fig. 7.

The initial temperature derived from fitting equation (1) to the averaged spectral curve of the observed hotspot is associated with the brightest pixel of the intensity map for an initial scale factor to invert the 700 nm intensity image into a temperature map. For each pixel of the temperature map thus obtained, a Planck curve is calculated. The collection of all Planck curves from all pixels is then averaged to obtain a synthetic version of the measured hotspot spectrum, which is then in turn converted into an intensity averaged spectrum. A Planck function is fitted against this synthetic spectrum using the same wavelength window that was originally used for the experimental spectrum. The assumed scale factor is then varied until the temperature obtained in this way from the intensity map corresponds to the observed equivalent. This represents the temperature map with correct absolute temperature values.

A single loop in this iterative procedure involves the computation of $\sim 30 \times 10^6$ Planck functions. In order to perform these calculations in quasi-real-time, we binned the total of 400 000 pixels of the temperature map into 100 equally spaced temperature bins corresponding to 100 Planck functions, which were weighted according to the number of elements in each bin. This reduced the computation time by roughly 3 orders of magnitude, thus allowing the final temperature map to be output in only seconds after data acquisition.

V. MEASURING THERMAL PRESSURE BY COMBINING HOTSPOT TEMPERATURE MAPS WITH X-RAY DIFFRACTION

As an example for the use of a realistic temperature map of the laser heated hotspot in a diamond anvil cell in combination with a small X-ray spot, we measure for the first time the spatially resolved pressure distribution around the laser-hotspot in a DAC.

A. Method

A symmetric DAC (Kantor *et al.*, 2012) equipped with 400 μm culet diamonds and cBN seats was loaded with 99.999% pure AgI powder (Sigma Aldrich, Product code 204404, lot no. 00724KE) using a Re gasket with a 150 μm hole in it. No pressure medium was added so that the sample was essentially single-phase, which simplifies the thermal pressure situation. The sample was pressurized to 3.8 GPa, which brought the AgI into its high-pressure phase III (NaCl structure).³² Room temperature pressures were determined using the volumetric bulk modulus derived from the pressure dependent volume data of Hull and Keen.³² There was no pressure gradient measurable across the sample. Also, we did not observe any pressure difference before and after laser heating; this observation is of key importance, as it implies that the sample heating occurred isochorically. At 3.8 GPa, the melting temperature is extrapolated to be approximately 1500 K also based on the phase diagram of Hull and Keen.³² AgI was chosen for this test experiment since its combination of low thermal conductivity (estimated to be <10 W/m K from Goetz and Cowen³³ and Håkansson and Andersson³⁴) and high emissivity (estimated to be >0.8 from data in Touloukian and DeWitt³¹) ensures extremely easy coupling with the IR laser even without any insulation from the diamonds. This makes precise positioning of the hotspot relative to the X-ray beam very reliable. A vertical diffraction transect (11 steps) across the centered hotspot (FWHM ~ 30 μm) was achieved by moving the DAC relative to the X-ray position in small steps while subsequently adjusting the hotspot back towards the sample center using the remote controlled laser mirrors. Diffraction exposures were only started after completion of the sample movement and re-centering of both laser positions. The laser power was held at 1 W or below which resulted in peak temperatures of around 1400 K. At each step, several temperature maps were created for both the upstream and downstream sides of the sample during the X-ray diffraction exposure. The X-ray positions relative to the temperature maps were determined by correlating the optical image of the gasket hole with the hotspot in its center with a 2-dimensional absorption map of the sample chamber and the known coordinates of the X-ray position within this absorption map.

X-ray diffraction experiments were performed on ALS beamline 12.2.2³⁵ using 25 keV X-rays focused to a 10 μm spot using a Kirkpatrick-Baez mirror setup and a Mar345 image plate at about 300 mm distance as a detector. Experimental parameters (sample to detector distance, detector tilt relative to incoming beam, X-ray energy) were refined based on a CeO₂ (NIST SRM 674b) powder diffraction pattern using Dioptas.³⁶ The observed cell volumes were extracted from the integrated diffraction patterns using the observed d-spacings of the 7 first observed lattice planes.

Thermal pressure values were deduced from the cell volume using a simplified approach as suggested by Helffrich and Connolly.³⁷ This assumes an exponential dependence of the bulk modulus K_0 with temperature parameterized through the Anderson-Grüneisen parameter δ ($\delta = -\frac{1}{\alpha K_0} (\frac{\partial K_0}{\partial T})_P$) and neglecting the temperature dependence of K' and α_0 (notably, the Debye temperature of AgI lies substantially below 500 K,³⁸

so its temperature dependence of thermal expansion is anticipated to be small at high temperatures). This allows us to express the temperature dependence of the bulk modulus as $K_T = K_0 \left[\frac{V_{00}}{V_{0T}} \right]^\delta$. Observing that $\delta \approx K' \approx 4$ additionally reduces the number of parameters. Assuming a constant thermal expansion, we calculate V_{0T} , which in turn allows us to obtain K_T for the temperature at the X-ray position. For the thermal expansion coefficient α_0 of AgI (III) in the rock-salt structure, we assumed the value of NaCl in the rock-salt structure ($\sim 8 \times 10^{-5} \text{ K}^{-1}$); our results scale directly with this assumed value. The temperature at the X-ray position is obtained from the observed temperature maps, where the values on the map were averaged over the size of the X-ray spot ($10 \mu\text{m}$). The temperatures of the upstream and downstream sample sides were averaged. The position on the temperature map was obtained from the X-ray absorption map with the assumption that the hotspot is centered on it. Utilizing V_{0T} and K_T as the reference volume and bulk modulus, respectively, we then convert the observed unit-cell volume (V_{PT}) to a total pressure using a second order (i.e., $K' = 4$) Murnaghan equation of state. All equation-of-state calculations were done using EosFit.³⁹ Based on the lack of pressure relaxation before and after laser-heating, the obtained pressure is assumed to be the sum of the static (cold) pressure plus the thermal pressure (P_{th}) created by the thermal expansion across the hotspot acting within a fixed volume.

B. Results: Distribution of thermal pressure in laser-heated AgI

In Table I, we list the volumes, temperatures, K_T , and deduced pressures for the 11 positions along a vertical transect through the hotspot. Positions are given in μm relative to the center of the hotspot (and thus center of gasket hole).

TABLE I. Results of thermal pressure calculations. See Sec. V A for details on calculations.

Position ^a	T ^b (K)	V_{0T} ^c (\AA^3)	K_T (GPa^{-1})	V_{PT} ^d (\AA^3)	P_{tot} ^e (GPa)	P_{th} ^f (GPa)
46	840	237.1	34.6	208.5	5.8	2.0
38	902	238.2	34.0	208.5	6.0	2.2
31	970	239.4	33.3	208.9	6.0	2.2
24	1071	241.3	32.3	208.8	6.3	2.5
16	1120	242.1	31.8	209.3	6.3	2.5
6	1400	247.2	29.2	209.8	6.8	3.0
1	1421	247.6	29.1	211.0	6.5	2.7
-4	1418	247.6	29.1	212.0	6.4	2.6
-18	1099	241.8	32.0	210.0	6.0	2.2
-26	1042	240.7	32.5	209.5	6.0	2.2
-33	1035	240.6	32.6	208.9	6.2	2.4

^aPositions here are given in μm relative to the center of the hotspot which is positioned at the center of the gasket hole.

^bThis is the temperature at the X-ray spot position given in column 1. The temperature is deduced from the temperature map. It is averaged over the size of the X-ray spot ($10 \mu\text{m}$) and also between upstream and downstream.

^c V_{0T} is calculated based on the measured temperature and an estimated coefficient of thermal expansion of $8 \times 10^{-5} \text{ K}^{-1}$ (value for NaCl rocksalt).

^d V_{PT} is derived from the observed *in situ* diffraction pattern at high P and T.

^e P_{tot} is derived from V_{PT} .

^f P_{th} is calculated as the difference of P_{tot} at P-T and P measured at room temperature.

Figure 8 shows the pressure profile across the hotspot with and without laser heating.

As can be seen from Table I and Fig. 8, we observe a rather homogenous pressure increase across the hotspot of $\sim 2\text{--}3 \text{ GPa}$. The center of the hotspot shows the highest pressures with a local pressure gradient of about $0.5 \text{ GPa}/10 \mu\text{m}$. If we compare our observed values with theoretical calculations by Heinz⁴⁰ and Dewaele, Fiquet, and Gillet,⁴¹ we find our values to be significantly smaller and with a smaller gradient than the values obtained by Heinz.⁴⁰ The absolute magnitude of this difference probably lies in the difference in thermoelastic properties between our relatively soft material, AgI, and Heinz' rather stiff model material (K_0 : 133 vs 41 GPa, G (shear modulus): 80 vs $\sim 10 \text{ GPa}$). Also, Heinz⁴⁰ did not take into account the temperature dependence of the bulk modulus. Dewaele, Fiquet, and Gillet⁴¹ performed finite element calculations on a model system consisting of a Si-oxide disk embedded in solid argon. Their peak values for the thermal pressure are of the same order of magnitude as what we observe. Their predicted pressure gradient is roughly $0.5 \text{ GPa}/10 \mu\text{m}$ in the sample, and about twice as steep in the solid Ar pressure medium. This is in quite good agreement with our measurements. An interesting difference with both the results of Heinz⁴⁰ and Dewaele, Fiquet, and Gillet⁴¹ is that in our experiment, the thermally induced pressure does not decrease to 0 even at the farthest distance ($\sim 60 \mu\text{m}$) from the hotspot. Instead, a thermal pressure of $\sim 2 \text{ GPa}$ seems to be maintained all the way to the edge of the gasket hole. This delocalization of thermal pressure seems to indicate that the material retains little shear strength (e.g., Shorr⁴²) at the high-temperatures of our experiment. This might indicate that the heated material had melted. However, our measured temperatures are $\sim 100\text{--}200 \text{ K}$ below the extrapolated melting temperature. These temperatures are, however, robustly in the range of the well-known fast-ionic diffusion state of AgI.^{43,44} Hence, the fast diffusion that characterizes this phase at high temperatures may produce rapid stress relaxation within this material and hence may be

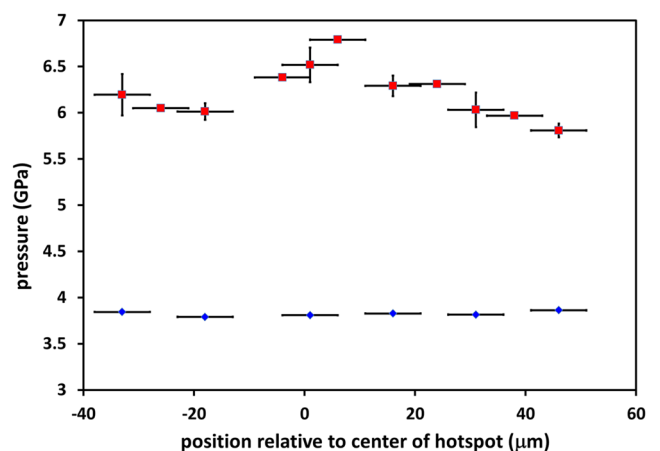


FIG. 8. Observed pressure across the hotspot/gasket hole with (red squares) and without (blue diamonds) laser heating, respectively. The pressure error bars do not take into account uncertainties in assumed thermoelastic properties but rather reflect the volume uncertainty obtained from the diffraction experiment. The horizontal bars represent the size of the beam. The positional error is about the size of the symbols.

manifested by an unresolvably small shear strength. A key aspect here is that the change in pressure far from the center of the hotspot is fully reversible on cooling, implying that the pressure elevation in regions where no visible glow is discernible is a robust feature associated with the heating within the hotspot, with the elevation in pressure equilibrating across a broad spatial range. Indeed, the anomaly for which we have no simple explanation is the modest (0.3–0.8 GPa) pressure elevation co-located with the hotspot; we speculate that the heat flow conditions are such that the overlying diamond may be undergoing heating and that this might induce this modest, localized pressure. Nevertheless, our observations clearly document that a well-calibrated and—corrected, highly stable laser-heating system can generate accurate measurements of both the magnitude and spatial distribution of thermal pressure within heated samples.

VI. CONCLUSIONS

The upgrade of the 12.2.2 double-sided laser heating system together with the implementation of improved temperature mapping capabilities based on modifications of the peak scaling method marks a significant step towards more reliable temperature measurements in the LHDAC while also maintaining the user friendliness and speed of data reduction that are optimal for a user-facility. It alleviates some of the long-standing issues associated with temperature measurements in LHDACs, such as chromatic aberration and difficult optical alignment on the hotspot peak. The relationship between the true peak temperature and the temperature fitted to the spectrum averaged over the entire hotspot is not constant even for a given sample, since it depends on fitting procedure (i.e., size and position of the wavelength window used for the Planck fit). An absolute temperature map can be determined iteratively by minimizing the difference between the observed fitted temperature and a modeled temperature fit based on the calculated temperature map to determine the correct scale factor. This enables quasi-real time temperature mapping while enabling interactive adjustments of the temperature fitting process (size and position of wavelength window employed, exposure time, and temperature dependent calibration). The accuracy of the method is confirmed through melting of metal (Ni, Pt, W) wires at ambient pressure. The availability of real temperature distributions in the LHDAC allows for more sophisticated interpretations of *in situ* laser heating experiments without relying on assumptions with respect to shape, size, and symmetry of the actual hotspot, all of which are strongly dependent on sample specific properties, such as grain size/heterogeneity, emissivity, sample to pressure medium ratio, the presence and nature of insulation material, etc.

The pressure profile through a laser heated hotspot on compressed AgI in its high-pressure rocksalt structure reveals deviations from theoretical predictions of thermal pressure across a laser-heated spot. These observations can help us to better characterize and understand thermal pressure in a LHDAC and ultimately offer an opportunity to extract additional information on thermoelastic properties at high pressure and high temperature.

Future work on system improvement will address the dynamic range of the imaging system through a combination of neutral density filters, laser beam expanders, and more powerful cameras; corresponding future work on thermal pressure will encompass materials with a wide range of high-temperature strengths and multi-phase sample assemblages.

ACKNOWLEDGMENTS

This publication is dedicated to the memory of Jason Knight, whose technical skills and invaluable friendship contributed to this work.

We thank the Advanced Light Source, which is supported by the Director, Office of Science, Office of Basic Energy Sciences, Materials Sciences Division, US Department of Energy under Contract No. DE-AC03-76SF00098 at Lawrence Berkeley National Laboratory and the University of California, Berkeley. COMPRES, the Consortium for Materials Properties Research in Earth Sciences, supported this project under NSF Cooperative Agreement No. EAR 16-49658 through funding of J.Y. and C.M.B. as well as for crucial beamline equipment. Q.W. was supported by NSF EAR-1620423.

- ¹Q. Williams, E. Knittle, and R. Jeanloz, *J. Geophys. Res.* **96**(B2), 2171–2184, <https://doi.org/10.1029/90jb01999> (1991).
- ²G. Fiquet, D. Andrault, A. Dewaele, T. Charpin, M. Kunz, and D. Häusermann, *Phys. Earth Planet. Inter.* **105**(1–2), 21–31 (1998).
- ³G. Shen, M. L. Rivers, Y. Wang, and S. R. Sutton, *Rev. Sci. Instrum.* **72**(2), 1273–1282 (2001).
- ⁴W. A. Bassett, *Rev. Sci. Instrum.* **72**(2), 1270–1272 (2001).
- ⁵W. Mao, G. Shen, V. B. Prakapenka, Y. Meng, A. J. Campbell, D. L. Heinz, J. Shu, R. J. Hemley, and H.-K. Mao, *Proc. Natl. Acad. Sci. U. S. A.* **101**(45), 15867–15869 (2004).
- ⁶L. Ismailova, E. Bykova, M. Bykov, V. Cerantola, C. McCammon, T. B. Ballaran, A. Bobrov, R. Sinmyo, N. Dubrovinskaia, and K. Glazyrin, *Sci. Adv.* **2**(7), e1600427 (2016).
- ⁷W. A. Caldwell, M. Kunz, R. Celestre, E. Domning, M. Walter, D. Walker, J. Glossinger, A. MacDowell, H. Padmore, and R. Jeanloz, *Nucl. Instrum. Methods Phys. Res., Sect. A* **582**(1), 221–225 (2007).
- ⁸H. Mao, P. Bell, J. Shaner, and D. Steinberg, *J. Appl. Phys.* **49**(6), 3276–3283 (1978).
- ⁹D. L. Heinz and R. Jeanloz, *J. Appl. Phys.* **55**(4), 885–893 (1984).
- ¹⁰S. Speziale, C. S. Zha, T. S. Duffy, R. J. Hemley, and H. K. Mao, *J. Geophys. Res.: Solid Earth* **106**(B1), 515–528, <https://doi.org/10.1029/2000jb900318> (2001).
- ¹¹L. C. Ming and W. A. Bassett, *Rev. Sci. Instrum.* **45**(9), 1115–1118 (1974).
- ¹²D. L. Heinz and R. Jeanloz, *High-Pressure Research in Mineral Physics: A Volume in Honor of Syun-iti Akimoto* (American Geophysical Union, 1987), pp. 113–127.
- ¹³A. J. Campbell, *Rev. Sci. Instrum.* **79**(1), 015108 (2008).
- ¹⁴M. J. Walter and K. T. Koga, *Phys. Earth Planet. Inter.* **143**, 541–558 (2004).
- ¹⁵L. R. Benedetti, D. L. Farber, and A. Kavner, *J. Appl. Phys.* **105**(2), 023517 (2009).
- ¹⁶L. R. Benedetti, N. Guignot, and D. L. Farber, *J. Appl. Phys.* **101**(1), 013109 (2007).
- ¹⁷J. Deng, Z. Du, L. R. Benedetti, and K. K. Lee, *J. Appl. Phys.* **121**(2), 025901 (2017).
- ¹⁸M. Manga and R. Jeanloz, *Geophys. Res. Lett.* **23**(14), 1845–1848, <https://doi.org/10.1029/96gl01602> (1996).
- ¹⁹A. Kavner and W. R. Panero, *Phys. Earth Planet. Inter.* **143**, 527–539 (2004).
- ²⁰A. Kavner and C. Nugent, *Rev. Sci. Instrum.* **79**(2), 024902 (2008).
- ²¹R. Boehler, *Rev. Geophys.* **38**(2), 221–245, <https://doi.org/10.1029/1998rg000053> (2000).
- ²²E. Rainey and A. Kavner, *J. Geophys. Res.: Solid Earth* **119**(11), 8154–8170, <https://doi.org/10.1002/2014jb011267> (2014).
- ²³MATLAB, R2016b, The MathWorks, Inc., Natick, Massachusetts, USA, 2016.

- ²⁴L. R. Benedetti and P. Loubeyre, *High Pressure Res.* **24**(4), 423–445 (2004).
- ²⁵S. Deemyad, A. N. Papathanassiou, and I. F. Silvera, *J. Appl. Phys.* **105**(9), 093543 (2009).
- ²⁶P. Lazor, G. Shen, and S. Saxena, *Phys. Chem. Miner.* **20**(2), 86–90 (1993).
- ²⁷L. S. Dubrovinsky and S. K. Saxena, *High Temp. - High Pressures* **31**(4), 393–399 (1999).
- ²⁸R. Jeanloz and A. Kavner, *Philos. Trans. R. Soc., A* **354**(1711), 1279–1305 (1996).
- ²⁹D. L. Heinz, J. S. Sweeney, and P. Miller, *Rev. Sci. Instrum.* **62**(6), 1568–1575 (1991).
- ³⁰A. P. Jephcoat and S. P. Besedin, *Philos. Trans. R. Soc., A* **354**(1711), 1333–1360 (1996).
- ³¹Y. Touloukian and D. DeWitt, *The TPRC Data Series* (IFI/Plenum Data Corporation, 1972), Vol. 8.
- ³²S. Hull and D. Keen, *Phys. Rev. B* **59**(2), 750 (1999).
- ³³M. Goetz and J. Cowen, *Solid State Commun.* **41**(4), 293–295 (1982).
- ³⁴B. Håkansson and P. Andersson, *J. Phys. Chem. Solids* **47**(4), 355–362 (1986).
- ³⁵M. Kunz, A. A. MacDowell, W. A. Caldwell, D. Cambie, R. S. Celestre, E. E. Domning, R. M. Duarte, A. E. Gleason, J. M. Glossinger, and N. Kelez, *J. Synchrotron Rad.* **12**(5), 650–658 (2005).
- ³⁶C. Prescher and V. B. Prakapenka, *High Pressure Res.* **35**(3), 223–230 (2015).
- ³⁷G. Helffrich and J. Connolly, *Am. Mineral.* **94**(11-12), 1616–1619 (2009).
- ³⁸K. S. Pitzer, *J. Am. Chem. Soc.* **63**(2), 516–518 (1941).
- ³⁹R. J. Angel, M. Alvaro, and J. Gonzalez-Platas, *Z. Kristallogr. - Cryst. Mater.* **229**(5), 405–419 (2014).
- ⁴⁰D. L. Heinz, *Geophys. Res. Lett.* **17**(8), 1161–1164, <https://doi.org/10.1029/g1017i008p01161> (1990).
- ⁴¹A. Dewaele, G. Fiquet, and P. Gillet, *Rev. Sci. Instrum.* **69**(6), 2421–2426 (1998).
- ⁴²B. F. Shorr, *Thermal Integrity in Mechanics and Engineering* (Springer, 2015).
- ⁴³J. Tallon, *Phys. Rev. B* **38**(13), 9069 (1988).
- ⁴⁴D. Keen, S. Hull, W. Hayes, and N. Gardner, *Phys. Rev. Lett.* **77**(24), 4914 (1996).